Chemical Science

ROYAL SOCIETY OF CHEMISTRY

EDGE ARTICLE

View Article Online
View Journal | View Issue

Check for updates

Cite this: *Chem. Sci.*, 2024, **15**, 18076

All publication charges for this article have been paid for by the Royal Society of Chemistry

High-performance deep-blue electroluminescence from multi-resonance TADF emitters with a spirofluorene-fused double boron framework†

Ke Xu, Nengquan Li, Zeyuan Ye, Yuxi Guo, Yuxin Wu, Chenghao Gui, Xiaojun Yin, Jingsheng Miao, Xiaosong Cao * and Chuluo Yang

Received 21st July 2024
Accepted 26th September 2024

DOI: 10.1039/d4sc04835k

rsc.li/chemical-science

The development of multi-resonance thermally activated delayed fluorescence (MR-TADF) materials in the deep-blue region is highly desirable. A usual approach involves constructing an extended MR-TADF framework; however, it may also intensify aggregate-caused quenching issues and thereby reduce device efficiency. In this study, we develop a molecular design strategy that fuses the MR-TADF skeleton with 9,9′-spirobifluorene (**SF**) units to create advanced deep-blue emitters. The **SF** moiety facilitates high-yield one-shot bora-Friedel–Crafts reaction towards an extended skeleton and mitigates interchromophore interactions as a steric group. Our findings reveal that orbital interactions at the fusion site significantly influence the electronic structure, and optimizing the fusion mode allows for the development of emitters with extended conjugation length while maintaining non-bonding character. The proof-of-concept emitter exhibits narrowband emission in the deep-blue region, a near-unity photoluminescence quantum yield, and a fast k_{RISC} of 2.4 × 10^5 s^{-1}. These exceptional properties enable the corresponding sensitizer-free OLED to achieve a maximum external quantum efficiency (EQE_{max}) of 39.0% and Commission Internationale de l'Eclairage (CIE) coordinates of (0.13, 0.09). Furthermore, the hyperfluorescence device realizes an EQE_{max} of 40.4% with very low efficiency roll-off.

Open Access Article. Published on 04 October 2024. Downloaded on 2/8/2026 12:44:33 AM.
This article is licensed under a Creative Commons Attribution-NonCommercial 3.0 Unported Licence.

Introduction

The recent conceptual advancements in molecular design have facilitated the transition of organic light-emitting diodes (OLED) from academic to commercial applications. To meet the increasing performance demands of ultrahigh-resolution displays, significant efforts have been directed towards enhancing the intrinsic color purity of organic emitters, while ensuring high efficiency and long-term operational stability. The inadequate color purity of current commercial emitters necessitates the development of new emitters with small linewidth. Recently, boron- and nitrogen-doped polycyclic heteroaromatics with multi-resonance thermally activated delayed fluorescence (MR-TADF) have garnered significant interest.[1,2] These emitters offer narrowband emissions even surpassing those of perovskite and quantum-dot light-emitting compounds.[3–5] The separation of the frontier molecular orbitals (FMOs) in these materials effectively suppresses structural relaxation and vibronic coupling, leading to high photoluminescence quantum yield (Φ_{PL}) and superior color purity. Numerous studies have since focused on revolutionizing molecular design and optimizing synthetic methodologies, significantly accelerating the development of MR-TADF materials for practical applications.

Among the efforts to modulate the optoelectronic properties of MR-TADF emitters, extending the π-skeleton has been identified as a cutting-edge strategic design, as theoretically predicted by Olivier *et al.*[6,7] This design principle has proven effective in increasing the reverse intersystem crossing rate constant (k_{RISC}), which is crucial for avoiding severe efficiency roll-off at high brightness.[8–10] The accelerated RISC is facilitated by short-range charge transfer (SR-CT) within the extended framework, resulting in a reduction in exchange energy. Importantly, with rational molecular design, the enlarged ring-fused structure can further promote the Φ_{PL} and generate even narrower emission linewidths. Consequently, multi-boron-embedded MR-TADF emitters currently outperform single boron-embedded MR-TADF materials in OLEDs.[11–20]

Nonetheless, the rigid planar structure of π-extended MR-TADF emitters can result in severe aggregation-caused quenching (ACQ) and spectral broadening in the solid state due to strong π–π interactions. As a result, a low doping ratio is typically employed during device fabrication to mitigate intermolecular interactions between chromophores, often leading to insufficient energy transfer and pronounced phase

Shenzhen Key Laboratory of New Information Display and Storage Materials, College of Materials Science and Engineering, Shenzhen University, Shenzhen 518060, China. E-mail: xcao@szu.edu.cn

† Electronic supplementary information (ESI) available. CCDC 2369010 2369013. For ESI and crystallographic data in CIF or other electronic format see DOI: https://doi.org/10.1039/d4sc04835k

© 2024 The Author(s). Published by the Royal Society of Chemistry

Open Access Article. Published on 04 October 2024. Downloaded on 2/8/2026 12:44:33 AM. This article is licensed under a Creative Commons Attribution-NonCommercial 3.0 Unported Licence.

separation.[21,22] Furthermore, achieving precise and consistent doping ratios adds complexity to production processes and increases manufacturing costs. To address this bottleneck, it is crucial to introduce steric hindrance into the extended fused-ring structure to specifically hinder intermolecular interactions and further improve OLED performance.[23–30]

To address this issue, we propose herein a 9,9′-spirobifluorene (**SF**)-fused strategy aimed at developing narrowband deep-blue emitters with high efficiency and low efficiency roll-off (Fig. 1). The incorporation of **SF** units serves a dual purpose: promoting π-electron delocalization and sterically shielding the emitting skeleton.[31] Unlike previous studies that attached bulky units to the MR-TADF core *via* a single bond, which may trigger undesirable structural relaxation during the electronic transition process, our approach yields emitters with high structural rigidity. It should be noted that embedding **SF** in the MR-TADF skeleton in a proper manner is challenging, as its π-bonding orbitals may deteriorate the non-bonding nature and enhance the conjugation length. Therefore, we designed two regioisomeric emitters to investigate the influence of fusion mode on the photophysical properties. Our results show that excellent emitters can be derived with extended conjugation length and well-retained non-bonding character by optimizing the fusion mode. Benefiting from the extended skeleton and suppressed chromophore interactions, the sensitizer-free device achieved maximum external quantum efficiencies (EQE_{max}) of up to 39.0% and a small full width at half maximum (FWHM) of 22 nm in the deep-blue region with Commission Internationale de l′Eclairage (CIE) coordinates of (0.13, 0.09). Moreover, with the assistance of a TADF sensitizer, the hyperfluorescent device achieved state-of-the-art efficiency with an $EQE_{max/1000}$ of 40.4% and 28.4%.

Molecular design, synthesis and characterization

As illustrated in Fig. 1, the **DB** featuring a double-boron-embedded framework was selected as the parent emitter due to its deep-blue emission and a relatively high k_{RISC} of 1.3×10^5 s^{-1}.[32,33] Additionally, the skeleton can be synthesized *via* a lithium-free bora-Friedel–Crafts reaction with good yield and can be easily derivatized by modifying the terminal aryl units of the amine precursor. The synthetic routes of **DB-SF1** and **DB-SF2** are similar and straightforward, as depicted in Scheme S1.† The corresponding precursors were synthesized through multi-step Buchwald–Hartwig C–N coupling reactions, and the final products were obtained *via* a one-shot borylation reaction with moderate yield (~40%) (Fig. S1–S11†). Notably, due to the high electrophilicity at the C2 position of **SF**, the borylation step of **DB-SF1** did not produce other possible regioisomers. Meanwhile, the large steric hindrance at the C1 position of **SF** also ensured the exclusive formation of **DB-SF2**. Both products were fully confirmed by NMR spectroscopy and high-resolution mass spectrometry (HR-MS), validating that the regioselectivity of the reacting sites greatly enhanced the synthetic yields of the targeted compounds. As shown in Fig. S12,† **DB-SF1** and **DB-SF2** exhibited significantly higher thermal decomposition temperatures (T_d, corresponding to a 5% weight loss) of 466 and 469 °C, respectively, compared to the parent molecule **DB** (386 °C), according to thermogravimetric analysis (TGA). Clearly, the introduction of **SF** contributes to better thermal stabilities and allows the emitters to be refined and further processed by vacuum sublimation.

To acquire a comprehensive understanding of the impact induced by the introduction of **SF** groups on molecular conformations and packing modes, single crystals of **DB-SF1** and **DB-SF2** were obtained by slow liquid diffusion of methanol into a chlorobenzene solution. Both emitters belonged to the triclinic space group *P*1, and the crystallographic data are summarized in Tables S1 and S2.† As displayed in Fig. 2, the linear π-extension of the **DB** core with **SF** moieties enhanced the overall structural planarity of both compounds but induced significant twisting at the molecular edges. Specifically, the spatial fluorene and mesitylene units displayed nearly perpendicular conformations with the MR-TADF skeleton, featuring dihedral angles in the range of 85.0° to 88.4°. The distorted geometry of the **DB** center remained intact in the presence of multiple B,N-doped-[4]helicenes, which not only mitigated intermolecular π–π stacking interactions but also triggered large spin–orbit coupling (SOC) and benefitted the RISC process

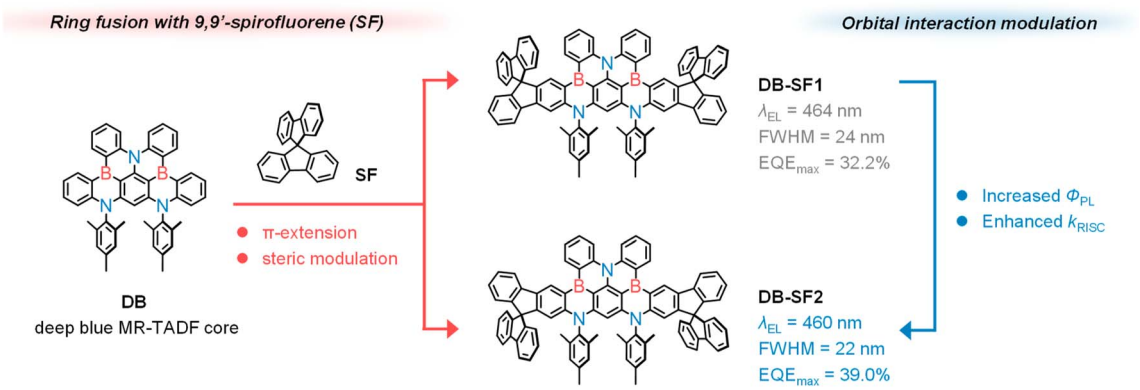

Fig. 1 Molecular design concept.

Open Access Article. Published on 04 October 2024. Downloaded on 2/8/2026 12:44:33 AM.
This article is licensed under a Creative Commons Attribution-NonCommercial 3.0 Unported Licence.

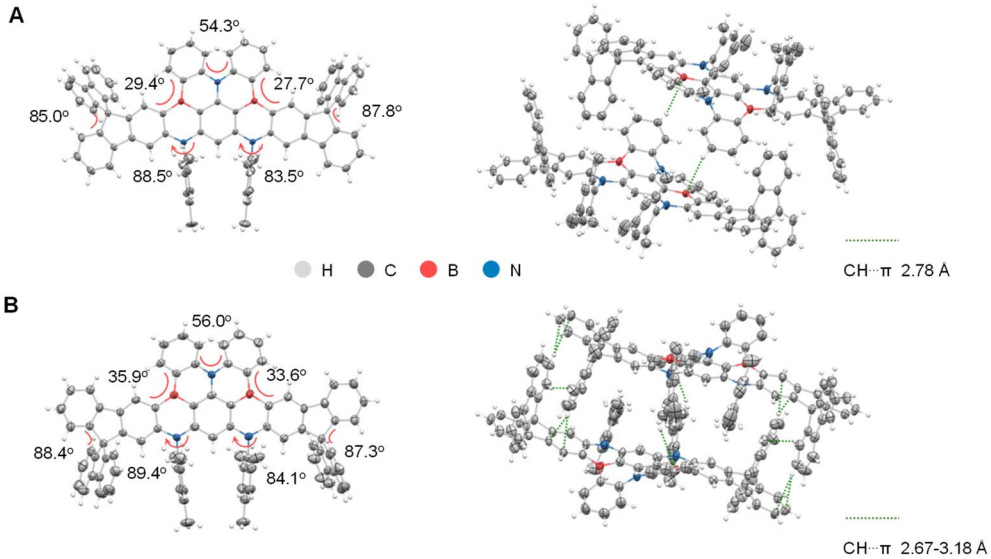

Fig. 2 Crystal structures and packing patterns of (A) **DB-SF1** and (B) **DB-SF2**.

according to previous reports.[34,35] The packing patterns indicated that the steric effect prevented the formation of π–π interactions between the dimers of **DB-SF1** and **DB-SF2**, enhancing the quenching-resistant properties of the emitters. Furthermore, adjacent molecules were interlocked *via* multiple C–H···π interactions below 3.2 Å, potentially minimizing non-radiative energy losses in the solid state.

Theoretical calculations

To unveil the effect of isomeric skeletons on the geometric and optoelectronic properties, we conducted analyses of their molecular orbitals using density functional theory (DFT) and time-dependent DFT (TD-DFT) at the B3LYP/6-31G(d,p) level (Fig. 3A and Tables S3–S7†). The electron density distributions on the HOMO were similar for both emitters, with **DB-SF2** showing slightly more extended delocalization to the fluorene segments. In contrast, their LUMO distributions differed significantly: **DB-SF2** primarily involved non-bonding orbitals across the fused-ring framework, suppressing undesired stretching vibrations, whereas **DB-SF1** exhibited hybridized π-bonding/non-bonding orbital characteristics. Clearly, the distinct π-bonding orbital on the boron and fluorene segments in **DB-SF1** weakened the resonance effect.[36] These findings thus suggested a significant influence of the fusion mode on the electron density distribution of FMOs, preserving desirable MR-TADF properties in **DB-SF2**. Consequently, both the HOMO and LUMO energy levels of **DB-SF2** were more destabilized than those of **DB-SF1**, and the net effect resulted in a higher energy bandgap (E_g) of **DB-SF2** (3.45 eV) compared to **DB-SF1** (3.37 eV).

To gain a deeper understanding of how the fusing site affects optoelectronic properties at the molecular level, the FMOs of **DB** and **SF** fragments were subsequently studied (Fig. 3A). The FMOs of **SF** exhibited a dominant π character on the biphenyls. In the fusion mode of **DB-SF1**, the C2(C3) atom of **DB** was linked with the C9(C5) atom of **SF**, respectively, while in the case of **DB-SF2**, the C3(C2) atom of **DB** was linked with the C9(C5) atom of **SF**. In a simplified manner, the different LUMO distributions between the two isomers can be understood as follows: in the case of **DB-SF2**, the C2 atom of **DB** could be regarded as a void position, perturbing the covalent π-bonding structure of the biphenyl site. In contrast, the C3 atoms of **DB** and the C5 atom of **SF** possessed the same bonding character in their LUMOs and thus could form a more delocalized π-conjugation, which deteriorated the MR-TADF character.

The natural transition orbitals (NTOs) (Fig. S14†) of S_1 closely resembled the FMO results, reflecting the electronic inertness of the spatial fluorene units. Consistent with the trend of E_gs, **DB-SF1** and **DB-SF2** exhibited S_1 energy levels of 2.89 eV and 2.96 eV, respectively. Despite the enlarged π-systems, the S_1 of **DB-SF2** only decreased moderately from **DB** (3.12 eV), indicating that the dominant non-bonding characters of the MR-TADF skeleton hindered effective conjugation length, thereby preserving deep-blue emission. Notably, **DB-SF2** showed reduced ΔE_{ST} values (0.36 eV) and increased f_{osc} values (0.6759) compared to **DB** (ΔE_{ST} = 0.41 eV, f_{osc} = 0.0618) and **DB-SF1** (ΔE_{ST} = 0.39 eV, f_{osc} = 0.0710), indicating enhanced SR-CT transition due to extended wavefunction delocalization and restricted π-bonding orbital formation. To account for electron correlation involving double excitations, we conducted higher-level RI-SCS-CC2 calculations to more accurately estimate excited-state energies.[6] These calculations produced smaller ΔE_{ST} values of 0.15 eV for **DB-SF1** and 0.09 eV for **DB-SF2** (Table S8†), which are consistent with the trends observed in TD-DFT calculations and show good agreement with the photophysical measurements. Furthermore, like **DB**, the two new emitters presented large spin–orbit coupling (SOC) values induced by the embedded twisted helicene subunits (*e.g.*, $\langle S_1|\hat{H}_{SOC}|T_1\rangle$ = 0.06 cm^{-1} and $\langle S_1|\hat{H}_{SOC}|T_2\rangle$ = 0.80 cm^{-1} for **DB-SF1**; $\langle S_1|\hat{H}_{SOC}|T_1\rangle$ = 0.10 cm^{-1} and $\langle S_1|\hat{H}_{SOC}|T_2\rangle$ = 0.91 cm^{-1} for **DB-**

© 2024 The Author(s). Published by the Royal Society of Chemistry

Open Access Article. Published on 04 October 2024. Downloaded on 2/8/2026 12:44:33 AM. This article is licensed under a Creative Commons Attribution-NonCommercial 3.0 Unported Licence.

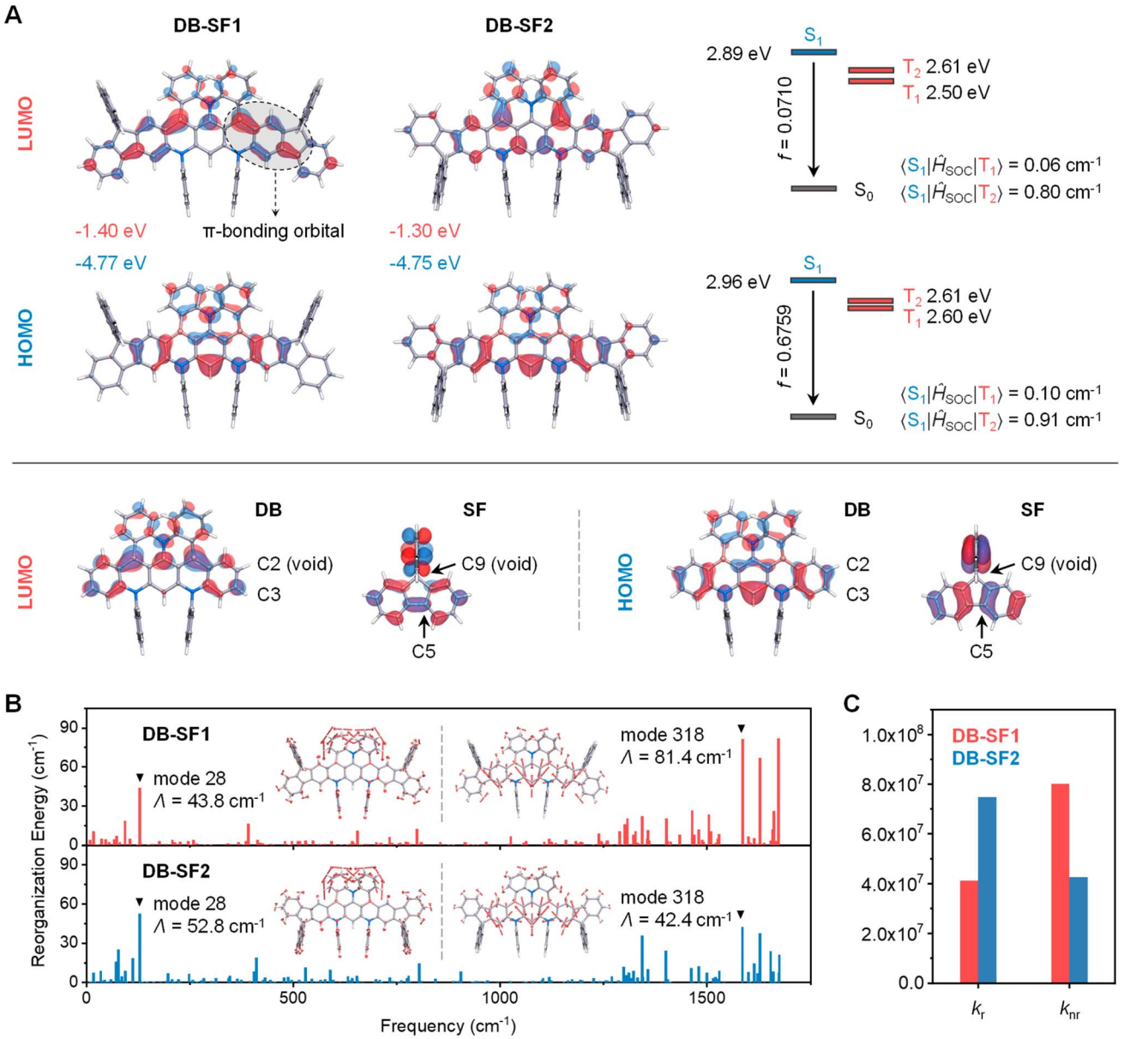

Fig. 3 (A) Top: distributions of highest occupied molecular orbital (HOMO, indicated by the blue isosurface) and lowest unoccupied molecular orbital (LUMO, indicated by the red isosurface) with associated energy levels, as well as the singlet/triplet state energy diagram and spin–orbit coupling (SOC) matrix elements of **DB-SF1** and **DB-SF2**; bottom: HOMO/LUMO distributions of the structural fragments **DB** and **SF**. (B) The reorganization energies (Λ) *versus* frequencies and the representative vibration modes for the $S_1 \rightarrow S_0$ transition of the emitters. (C) Simulated radiative (k_r) and non-radiative rate constants (k_{nr}) of the emitters.

SF2, with T_2 close to S_1 and T_1 for both emitters). These significant SOC matrix elements were expected to convert into high k_{RISC}s according to Fermi's golden rule.[37–39]

Next, the reorganization energy (Λ) and Huang-Rhys factors (HRF) of **DB-SF1** and **DB-SF2** were simulated and analyzed based on the optimal S_0 and S_1 geometries using the molecular materials property prediction package (MOMAP, Fig. 3B). The structural relaxation during the excitation-emission process was more suppressed in **DB-SF2**, as indicated by its apparent reduction of total Λ (1506 cm^{-1}) compared to **DB-SF1** (1836 cm^{-1}). The relationships of Λ with normal vibration modes for the $S_1 \rightarrow S_0$ transition showed that although the intensities of low-frequency vibrations between the two emitters were comparable, **DB-SF2** exhibited much suppressed vibronic coupling strength of high-frequency modes around 1500 cm^{-1}. These dominant high-frequency modes were associated with the stretching of C–C bonds across the entire molecular framework, and the intensity decrease in **DB-SF2** was attributed to its predominantly non-bonding character. Ultimately, the reduced Λ combined with increased f_{osc} translated into a larger radiative rate constant (k_r) and a smaller non-radiative rate constant (k_{nr}) in **DB-SF2**, as illustrated in Fig. 3C. These findings confirmed that the orbital interactions at the fusion site within

Open Access Article. Published on 04 October 2024. Downloaded on 2/8/2026 12:44:33 AM. This article is licensed under a Creative Commons Attribution-NonCommercial 3.0 Unported Licence.

these emitters played a decisive role in their electronic structure.

Photophysical properties

The photophysical properties in dilute toluene solution (1×10^{-5} M) were subsequently characterized, with the results displayed in Fig. 4 and summarized in Table 1. Both emitters' absorption spectra featured a combination of n–π*/π–π* transitions (below 400 nm) and intense SR-CT bands (above 400 nm). Based on the onsets of the absorption spectra, the optical E_g of **DB-SF1** (2.71 eV) was estimated to be marginally higher than that of **DB-SF2** (2.69 eV). Correspondingly, the solution fluorescence spectra of **DB-SF2** displayed a blue-shifted emission maximum (457 nm) compared to **DB-SF1** (461 nm). The minimized Stokes shift ($\Delta\lambda = 0.07$ eV) in **DB-SF2** indicated a lower reorganization energy between the ground and excited state configurations than **DB-SF1** ($\Delta\lambda = 0.10$ eV). For the same reason, **DB-SF2** exhibited a smaller FWHM value (21 nm) with a reduced intensity of the low-energy peak shoulder than that of **DB-SF1** (FWHM = 22 nm). Such spectral profile rendered **DB-SF2** ($CIE_y = 0.076$) with better color purity compared to **DB-SF1** ($CIE_y = 0.097$) (Fig. S15A†). Furthermore, we investigated the fluorescence spectra in different polar solvents. When varying the solvents from *n*-hexane to dichloromethane, the FWHMs for both emitters remained narrow, and the solvatochromic effect was moderate, indicating SR-CT characteristics (Fig. S16 and Table S9†). To estimate the key energy levels of the two molecules, we measured their fluorescence and phosphorescence spectra in frozen toluene at 77 K (Fig. 4B). The S_1/T_1 energy levels for **DB-SF1** were determined to be 2.68/2.48 eV and for **DB-SF2** as 2.72/2.55 eV based on the peak maxima of fluorescence and phosphorescence, resulting in ΔE_{ST} values of 0.20/0.17 eV. The smaller ΔE_{ST} value for **DB-SF2** suggested its potential for a more effective triplet exciton upconversion process.

To verify the TADF properties, doped films (2 wt% in polymethyl methacrylate, PMMA) were prepared. The associated kinetic parameters are summarized in Table 1. Both emitters exhibited similar fluorescence spectra compared to their toluene solutions, despite slightly broadened emission bands caused by the microenvironment change (Fig. S17†). The steric hindrance groups minimized molecular aggregation, resulting in good Φ_{PL} values (81% for **DB-SF1** and 95% for **DB-SF2**). Temperature-dependent transient decay curves (Fig. 4C and D) revealed that **DB-SF1** and **DB-SF2** in doped films exhibited pure TADF character with clear bi-exponential decay. The delayed components intensified as the temperature increased. Notably, **DB-SF2** demonstrated a much shorter delayed lifetime of 10.1 μs compared to **DB-SF1's** 22.3 μs at room temperature. This shorter lifetime rendered a more rapid k_{RISC} of 2.4×10^5 s^{-1} for **DB-SF2** *versus* 1.0×10^5 s^{-1} for **DB-SF1**, nearly double that of the parent **DB** molecule ($k_{RISC} = 1.3 \times 10^5$ s^{-1}). Further analysis

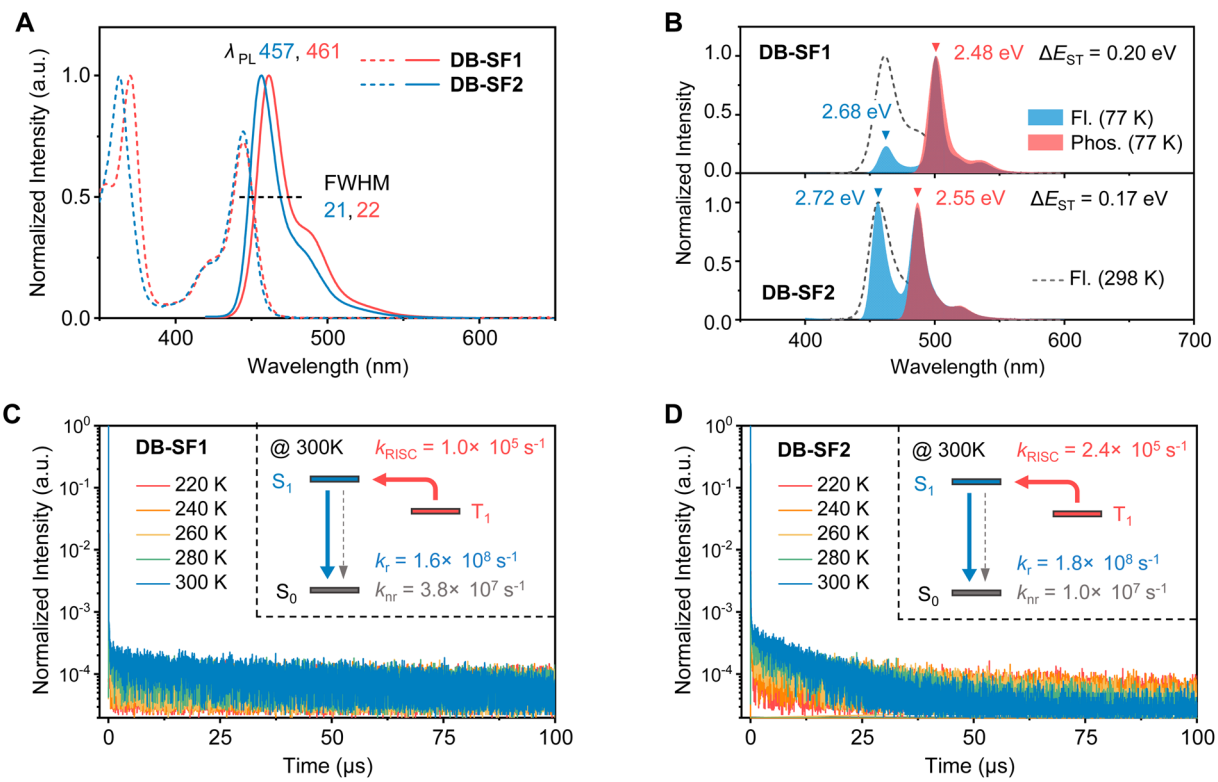

Fig. 4 (A) UV-vis absorption and normalized fluorescence spectra recorded at 298 K; (B) normalized fluorescence at 298 K and 77 K, as well as phosphorescence spectra recorded at 77 K of the emitters in toluene solution (1×10^{-5} M). Transient photoluminescence decay curves of (C) **DB-SF1** and (D) **DB-SF2** in 2 wt% polymethyl methacrylate (PMMA) doped films at varied temperatures (inset: schematic illustration of radiative/non-radiative decay, and reverse intersystem crossing processes with calculated rate constants).

© 2024 The Author(s). Published by the Royal Society of Chemistry

Open Access Article. Published on 04 October 2024. Downloaded on 2/8/2026 12:44:33 AM. This article is licensed under a Creative Commons Attribution-NonCommercial 3.0 Unported Licence.

Table 1 Photophysical data of the emitters

Emitter	λ_{abs}[a] (nm)	λ_{em}[a] (nm)	FWHM[a] (nm meV^{-1})	ΔE_{ST}[b] (eV)	Φ_{PL}[c] (%)	Φ_{PF}[c] (%)	Φ_{DF}[c] (%)	τ_{PF}[d] (ns)	τ_{DF}[d] (μs)	k_r[e] (10^8 s^{-1})	k_{nr}[e] (10^6 s^{-1})	k_{RISC}[e] (10^5 s^{-1})
DB-SF1	445	461	22/130	0.20	81	36	45	2.2	22.3	1.6	38.0	1.0
DB-SF2	445	457	21/125	0.17	95	40	55	2.2	10.1	1.8	9.6	2.4

[a] Peak of absorption (λ_{abs}) and fluorescence (λ_{em}, 298 K) spectra, as well as color coordinates in the CIE 1931 chromaticity diagram and full-width at half-maximum (FWHM) of fluorescence. [b] S_1-T_1 energy gap (ΔE_{ST}) determined from the onset of low-temperature fluorescence and phosphorescence spectra measured in 1×10^{-5} M toluene solution. [c] Absolute photoluminescence quantum yield (Φ_{PL}), and quantum yields of prompt and delayed fluorescence (Φ_{PF} and Φ_{DF}). [d] Lifetimes of prompt and delayed fluorescence (τ_{PF} and τ_{DF}), the percentage value given in parentheses refers to the fractional intensity. [e] Rate constants of singlet radiative decay (k_r), non-radiative decay (k_{nr}), intersystem crossing (k_{ISC}), and reverse intersystem crossing (k_{RISC}) measured in the PMMA film with 2 wt% doping ratio.

showed that **DB-SF2** exhibited a faster k_r of 1.8×10^8 s^{-1} and a smaller k_{nr} of 9.6×10^6 s^{-1} compared to **DB-SF1** ($k_r = 1.6 \times 10^8$ s^{-1}, $k_{nr} = 3.8 \times 10^7$ s^{-1}), as deduced from the transient decay curves and Φ_{PL} values. The combination of higher Φ_{PL} values, shorter delayed lifetimes, and more efficient k_{RISC} and k_r rates in **DB-SF2** underscores its superior TADF properties compared to **DB-SF1** and the parent **DB** molecule, confirming the effectiveness in molecular design. These advantages arose from the promoted π-electron delocalization and prevalent non-bonding orbital character in **DB-SF2**, consistent with *in silico* predictions.

Electroluminescent properties

To assess the electroluminescent (EL) performance, we fabricated and characterized devices based on a structure comprising ITO/HAT-CN (5 nm)/TAPC (30 nm)/TCTA (15 nm)/mCBP (20 nm)/SiTrzCz2: *x* wt% **DB-SF1** or **DB-SF2** (25 nm)/SiTrzCz2 (10 nm)/ANT-BIZ (30 nm)/Liq (2 nm)/Al (100 nm). In this structure, ITO (indium tin oxide) and Al (aluminum) served as the anode and cathode, respectively. HAT-CN (dipyrazino[2,3-*f*:2′,3′-*h*]quinoxaline-2,3,6,7,10,11-hexacarbonitrile) and Liq (8-quinolinolato lithium) functioned as hole- and electron-injection layers, respectively. TAPC (1,1-bis((di-4-tolylamino) phenyl)-cyclohexane) and TCTA (4,4′,4″-tris(*N*-carbazolyl)-triphenylamine) served as hole-transporting layers, while ANT-BIZ (1-(4-(10-([1,1′-biphenyl]-4 yl)anthracen-9-yl)phenyl)-2-ethyl-1*H*-benzo[*d*]imidazole) acted as the electron-transporting layer. mCBP (3,3-di(9H-carbazol-9-yl)biphenyl) was employed as the exciton-blocking layer. SiTrzCz2 (9,9′–(6-(3-(triphenylsilyl)phenyl)-1,3,5-triazine-2,4-diyl)bis(9*H*-carbazole)) was chosen as the host material due to its matched energy levels with adjacent functional layers, suitable triplet energy level, and appropriate spectral overlap between the host emission and dopant absorption. The device configurations and performances are depicted in Fig. 5 (the HOMO/LUMO levels of **DB-SF1** and **DB-SF2** in the energy level diagram were deduced by cyclic voltammetry (CV) measurements and absorption onset values, Fig. S13†), with key EL parameters summarized in Table 2.

The doping ratio of **DB-SF1** or **DB-SF2** in the emitting layer (EML) was adjusted from 1 to 8 wt% to evaluate concentration-dependent characteristics (Fig. S18, S19 and Table S10†). The EQE_{max} and FWHM *versus* dopant concentration relationships are shown in Fig. 5B. For both emitters, energy transfer was not complete until the 5 wt% doping ratio, and the maximum device efficiency was achieved at this point. In the 1–5 wt% range, the spectra of **DB-SF1** showed a marginal red-shift of the emission maxima from 461 to 464 nm with negligibly increased FWHMs from 22 to 24 nm. Similarly, a small FWHM increase from 21 nm (1 wt%, $\lambda_{EL} = 459$ nm) to 22 nm (5 wt%, $\lambda_{EL} = 460$ nm) was recorded for **DB-SF2**. Although further concentration increases can induce the formation of detrimental aggregates/excimers, leading to declined efficiency and color purity, it is noteworthy that previously reported π-extended MR-TADF emitters (such as *ν*-DABNA) typically required less than 2 wt% to achieve optimal device performance.[11,40] Thus, the relative concentration independence for both emitters validates the feasibility of our molecular design strategy for spatial regulation. Remarkably, efficient OLED performances were realized without light out-coupling technologies, offering EQE_{max} values of 32.2% and 39.0% for **DB-SF1** and **DB-SF2** at 5 wt%, accompanied by high maximum current efficiency (CE_{max}) of 34.5 and 31.6 cd A^{-1}, respectively. The corresponding CIE coordinates were (0.13, 0.12) for **DB-SF1** and (0.13, 0.09) for **DB-SF2**, with the latter approaching the blue point (0.14, 0.08) defined by the National Television System Committee (NTSC). The significantly higher EQE_{max} value of **DB-SF2** was associated with its improved Φ_{PL}, while the better CE_{max} of **DB-SF1** could be attributed to its red-shifted EL spectrum. With a more efficient RISC process and therefore reduced triplet exciton density, **DB-SF2** also showed moderate efficiency roll-off behavior at practical luminance, maintaining an EQE of 20.7% at a luminance of 1000 cd m^{-2}, which was significantly higher than that of **DB-SF1** (6.1% at 1000 cd m^{-2}). As another crucial parameter, operational stability was subsequently assessed using OLEDs with a 5 wt% doping ratio (Fig. S20†). **DB-SF2** manifested a 2.3-fold increase in operational half-life (LT_{50} of 88.6 h) at an initial luminance of 100 cd m^{-2} compared to **DB-SF1** (LT_{50} of 38.5 h). Given the similar emission energies of the two emitters, the enhanced stability of **DB-SF2** is attributed to its superior triplet-harvesting capability. These results highlight the importance of optimizing orbital interactions at the fusion site to minimize detrimental π-bonding character in deep-blue emitters.

To further enhance EL performance, hyperfluorescence (HF) OLEDs were fabricated with a structure of ITO/HATCN (5 nm)/TAPC (30 nm)/TCTA (15 nm)/mCBP (10 nm)/EML (25 nm)/DPFPO (10 nm)/ANT-BIZ (30 nm)/Liq (1 nm)/Al (150 nm). The

Open Access Article. Published on 04 October 2024. Downloaded on 2/8/2026 12:44:33 AM.
This article is licensed under a Creative Commons Attribution-NonCommercial 3.0 Unported Licence.

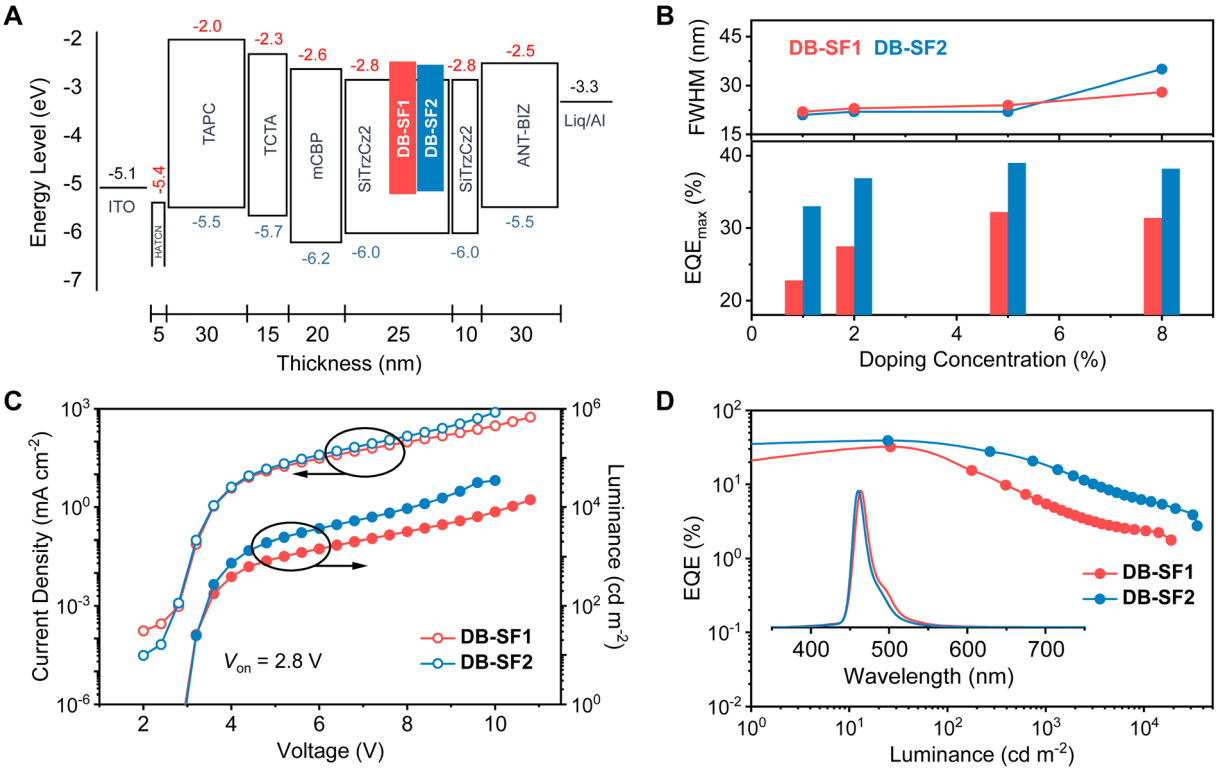

Fig. 5 (A) Device configurations and energy-level diagrams of the non-sensitized devices. (B) Maximum external quantum efficiency (EQE_{max}) and full width at half maximum (FWHM) *versus* dopant concentration relationships of the devices. (C) Current density–voltage–luminance curves and (D) EQE-luminance curves of **DB-SF1** and **DB-SF2**-based OLEDs with 5 wt% doping ratio (inset: electroluminescence spectra at 6 V).

EML was a ternary blended film DBFPO: 20 wt% mMDBA-DI: 2 wt% emitters (Fig. 6A), where mMDBA-DI (5-(3,11-dimethyl-5,9-dioxa-13*b*-boranaphtho[3,2,1-*de*]anthracen-7-yl)-10,15-diphenyl-10,15-dihydro-5*H*-diindolo[3,2-*a*:3′,2′-*c*]carbazole) was selected as a sensitizer due to its well-matched PL spectra (Fig. S21A†) with the absorption spectra and high k_{RISC}. Meanwhile, DBFPO (2,8-bis(diphenylphosphoryl)dibenzo[*b*,*d*]furan) was employed as the host and hole/exciton-blocking material due to its higher T_1 energy. In this device configuration, the generated triplet excitons were harvested by the sensitizer and then transferred to the terminal emitter through efficient long-range Förster resonance energy transfer (FRET). Combined with the close-to-unity Φ_{PL} and large k_r of **DB-SF2**, the HF device exhibited notable improvement in device efficiency while retaining narrowband emission (Fig. 6B, S21 and S22†). The EL spectrum was slightly red-shifted with emission peaking at 462 nm, an FWHM of 29 nm, and CIE coordinates of (0.13, 0.13), due to the large polarity of DBFPO and mMDBA-DI mixed matrixes. An impressive EQE_{max} of 40.4% was achieved, along with a CE_{max} of 45.1 cd A^{-1}, representing one of the highest efficiencies among reported OLED devices based on blue MR-TADF materials. Furthermore, this device showed alleviated roll-offs, maintaining an EQE of 28.4% at a luminance of 1000 cd m^{-2}. It is noteworthy that while **DB-SF2** primarily served as a fluorescence emitter in this HF device, the triplet population on the terminal emitter was still possible. In this regard, the fast RISC process of **DB-SF2** remained beneficial herein. For comparison, the HF device based on **DB-SF1** exhibited inferior EQE_{max} and more pronounced roll-off, underscoring the advantage of the higher k_{RISC} of **DB-SF2**.

Table 2 Summary of the key device data

Device (emitter)	V_{on}[a] (V)	λ_{EL}[b] (nm)	FWHM[c] (nm meV^{-1})	L_{max}[d] (cd m^{-2})	$CE_{max/1000}$[e] (cd A^{-1})	$EQE_{max/1000}$[f] (%)	CIE[g] (x, y)
DB-SF1	2.8	464	24/135	18 911	34.5/5.7	32.2/6.1	(0.13, 0.12)
DB-SF2	2.8	460	22/129	34 851	31.6/16.8	39.0/20.7	(0.13, 0.09)
DB-SF1 HF	3.2	468	32/179	14 048	42.3/18.5	34.2/15.1	(0.13, 0.16)
DB-SF2 HF	3.2	462	29/168	26 163	45.1/30.2	40.4/28.4	(0.13, 0.13)

[a] Turn-on voltage recorded at the luminance of 1 cd m^{-2}. [b] Maximum EL wavelength. [c] FWHM of EL spectra. [d] Maximum brightness. [e] Current efficiency at maximum and 1000 cd m^{-2}. [f] Efficiency at maximum and 1000 cd m^{-2}. [g] EL color coordinates in the CIE 1931 chromaticity diagram recorded at 6 V.

© 2024 The Author(s). Published by the Royal Society of Chemistry

Open Access Article. Published on 04 October 2024. Downloaded on 2/8/2026 12:44:33 AM.
This article is licensed under a Creative Commons Attribution-NonCommercial 3.0 Unported Licence.

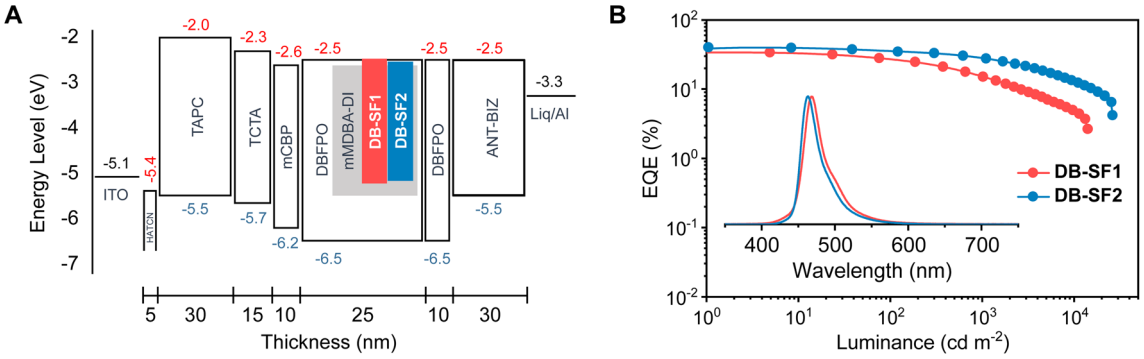

Fig. 6 (A) Device configurations and energy-level diagrams of the hyperfluorescence (HF) devices. (B) EQE-luminance curves with electroluminescence spectra at 6 V as the inset.

Conclusion

In summary, we designed and constructed an isomeric pair of deep-blue MR-TADF emitters, **DB-SF1** and **DB-SF2**, by fusing a double-boron embedded framework with 9,9′-spirobifluorene. This approach aimed to extend π-conjugated skeletons while mitigating interchromophore quenching issues. Theoretical simulations and photophysical measurements highlighted the crucial role of orbital interactions between fused-ring segments on the electronic structure, providing a guideline for modulating π-bonding and non-bonding orbital features. Due to enhanced π-electron delocalization and well-retained non-bonding character, **DB-SF2** exhibited hypsochromic shifted emission, smaller reorganization energy, and a reduced ΔE_{ST} compared to **DB-SF1**. These attributes led to a near-unity Φ_{PL} and a fast RISC process ($k_{RISC} = 2.4 \times 10^5\ s^{-1}$) for **DB-SF2** in the deep-blue region in the solid state, demonstrating the effectiveness of π-extension combined with structural steric hindrance improvement. Benefitting from its excellent MR-TADF properties, the non-sensitized device based on **DB-SF2** exhibited narrowband electroluminescence (FWHM = 22 nm) with CIE coordinates of (0.13, 0.09) and $EQE_{max/1000}$ of 39.0%/20.7%. The remarkable device efficiency surpassed those of the previously reported binary deep-blue OLEDs with $CIE_y < 0.12$ (Table S11†). Additionally, the hyperfluorescent OLED demonstrated a further improved EQE_{max} of 40.4% and a lower efficiency roll-off at high luminance ($EQE_{1000} = 28.4\%$). Our design strategy thus provides a promising pathway to achieve high-performance narrowband blue MR-TADF emitters, aligning with the requisites of ultrahigh-definition OLED displays.

Data availability

All data supporting the findings of this study are presented in the article and ESI.† Additional data are available from the corresponding author upon reasonable request.

Author contributions

X. Cao conceived the idea and supervised the project. K. Xu wrote the original draft. X. Cao and C. Yang reviewed and edited the manuscript. K. Xu, Y. Wu, C. Gui and X. Yin conducted the synthesis, basic property characterization, and theoretical calculations. N. Li performed the fabrication and characterization of the devices. Z. Ye and J. Miao analysed the data. All the authors participated in the discussion of the results.

Conflicts of interest

There are no conflicts to declare.

Acknowledgements

We acknowledge financial support from the National Natural Science Foundation of China (22375130, 52130308, and 52373192), the Shenzhen Science and Technology Program (JCYJ20230808105603008), the Research Team Cultivation Program of Shenzhen University (2023DFT004), and the Guangdong Basic and Applied Basic Research Foundation (2024A1515030199). We also thank the Instrumental Analysis Center of Shenzhen University for analytical support.

References

1 T. Hatakeyama, K. Shiren, K. Nakajima, S. Nomura, S. Nakatsuka, K. Kinoshita, J. Ni, Y. Ono and T. Ikuta, *Adv. Mater.*, 2016, **28**, 2777–2781.
2 S. Madayanad Suresh, D. Hall, D. Beljonne, Y. Olivier and E. Zysman-Colman, *Adv. Funct. Mater.*, 2020, **30**, 1908677.
3 Y. Liu, J. Cui, K. Du, H. Tian, Z. He, Q. Zhou, Z. Yang, Y. Deng, D. Chen, X. Zuo, Y. Ren, L. Wang, H. Zhu, B. Zhao, D. Di, J. Wang, R. H. Friend and Y. Jin, *Nat. Photonics*, 2019, **13**, 760–764.
4 T.-H. Han, K. Y. Jang, Y. Dong, R. H. Friend, E. H. Sargent and T.-W. Lee, *Nat. Rev. Mater.*, 2022, **7**, 757–777.
5 T. Kim, K.-H. Kim, S. Kim, S.-M. Choi, H. Jang, H.-K. Seo, H. Lee, D.-Y. Chung and E. Jang, *Nature*, 2020, **586**, 385–389.
6 A. Pershin, D. Hall, V. Lemaur, J.-C. Sancho-Garcia, L. Muccioli, E. Zysman-Colman, D. Beljonne and Y. Olivier, *Nat. Commun.*, 2019, **10**, 597.
7 Y.-J. Pu, D. Valverde, J. C. Sancho-García and Y. Olivier, *J. Phys. Chem. A*, 2023, **127**, 10189–10196.

Open Access Article. Published on 04 October 2024. Downloaded on 2/8/2026 12:44:33 AM. This article is licensed under a Creative Commons Attribution-NonCommercial 3.0 Unported Licence.

8 K. R. Naveen, H. I. Yang and J. H. Kwon, *Commun. Chem.*, 2022, **5**, 149.
9 H. Jiang, J. Jin and W.-Y. Wong, *Adv. Funct. Mater.*, 2023, **33**, 2306880.
10 X.-F. Luo, X. Xiao and Y.-X. Zheng, *Chem. Commun.*, 2024, **60**, 1089–1099.
11 Y. Kondo, K. Yoshiura, S. Kitera, H. Nishi, S. Oda, H. Gotoh, Y. Sasada, M. Yanai and T. Hatakeyama, *Nat. Photonics*, 2019, **13**, 678–682.
12 Y. Sano, T. Shintani, M. Hayakawa, S. Oda, M. Kondo, T. Matsushita and T. Hatakeyama, *J. Am. Chem. Soc.*, 2023, **145**, 11504–11511.
13 S. Uemura, S. Oda, M. Hayakawa, R. Kawasumi, N. Ikeda, Y.-T. Lee, C.-Y. Chan, Y. Tsuchiya, C. Adachi and T. Hatakeyama, *J. Am. Chem. Soc.*, 2023, **145**, 1505–1511.
14 J. Jin, C. Duan, H. Jiang, P. Tao, H. Xu and W.-Y. Wong, *Angew. Chem., Int. Ed.*, 2023, **62**, e202218947.
15 X.-C. Fan, F. Huang, H. Wu, H. Wang, Y.-C. Cheng, J. Yu, K. Wang and X.-H. Zhang, *Angew. Chem., Int. Ed.*, 2023, **62**, e202305580.
16 X. Cai, Y. Pu, C. Li, Z. Wang and Y. Wang, *Angew. Chem., Int. Ed.*, 2023, **62**, e202304104.
17 K. R. Naveen, J. H. Oh, H. S. Lee and J. H. Kwon, *Angew. Chem., Int. Ed.*, 2023, **62**, e202306768.
18 Y. Zhang, J. Wei, L. Wang, T. Huang, G. Meng, X. Wang, X. Zeng, M. Du, T. Fan, C. Yin, D. Zhang and L. Duan, *Adv. Mater.*, 2023, **35**, 2209396.
19 X. Huang, J. Liu, Y. Xu, G. Chen, M. Huang, M. Yu, X. Lv, X. Yin, Y. Zou, J. Miao, X. Cao and C. Yang, *Natl. Sci. Rev.*, 2024, **11**, nwae115.
20 L. Yuan, J.-W. Xu, Z.-P. Yan, Y.-F. Yang, D. Mao, J.-J. Hu, H.-X. Ni, C.-H. Li, J.-L. Zuo and Y.-X. Zheng, *Angew. Chem., Int. Ed.*, 2024, **63**, e202407277.
21 H. Liu, J. Zeng, J. Guo, H. Nie, Z. Zhao and B. Z. Tang, *Angew. Chem., Int. Ed.*, 2018, **57**, 9290–9294.
22 Y. Xu, Z. Cheng, Z. Li, B. Liang, J. Wang, J. Wei, Z. Zhang and Y. Wang, *Adv. Opt. Mater.*, 2020, **8**, 1902142.
23 Y. Xu, C. Li, Z. Li, Q. Wang, X. Cai, J. Wei and Y. Wang, *Angew. Chem., Int. Ed.*, 2020, **59**, 17442–17446.
24 P. Jiang, J. Miao, X. Cao, H. Xia, K. Pan, T. Hua, X. Lv, Z. Huang, Y. Zou and C. Yang, *Adv. Mater.*, 2022, **34**, 2106954.
25 Y. Zhang, J. Wei, D. Zhang, C. Yin, G. Li, Z. Liu, X. Jia, J. Qiao and L. Duan, *Angew. Chem., Int. Ed.*, 2022, **61**, e202113206.
26 Y.-K. Qu, D.-Y. Zhou, F.-C. Kong, Q. Zheng, X. Tang, Y.-H. Zhu, C.-C. Huang, Z.-Q. Feng, J. Fan, C. Adachi, L.-S. Liao and Z.-Q. Jiang, *Angew. Chem., Int. Ed.*, 2022, **61**, e202201886.
27 T. Fan, Y. Zhang, L. Wang, Q. Wang, C. Yin, M. Du, X. Jia, G. Li and L. Duan, *Angew. Chem., Int. Ed.*, 2022, **61**, e202213585.
28 F.-M. Liu, Z.-H. Qu, P. Zuo, Y.-J. Yu, M.-T. Li, L.-S. Liao, D.-Y. Zhou and Z.-Q. Jiang, *ACS Mater. Lett.*, 2024, **6**, 1380–1387.
29 X.-F. Luo, H.-X. Ni, X. Liang, D. Yang, D. Ma, Y.-X. Zheng and J.-L. Zuo, *Adv. Opt. Mater.*, 2023, **11**, 2203002.
30 E. Ravindran, H. E. Baek, H. W. Son, J. H. Park, Y.-H. Kim and M. C. Suh, *Adv. Funct. Mater.*, 2023, **33**, 2213461.
31 Y.-K. Qu, Q. Zheng, J. Fan, L.-S. Liao and Z.-Q. Jiang, *Acc. Mater. Res.*, 2021, **2**, 1261–1271.
32 K. Matsui, S. Oda, K. Yoshiura, K. Nakajima, N. Yasuda and T. Hatakeyama, *J. Am. Chem. Soc.*, 2018, **140**, 1195–1198.
33 Z. Ye, H. Wu, Y. Xu, T. Hua, G. Chen, Z. Chen, X. Yin, M. Huang, K. Xu, X. Song, Z. Huang, X. Lv, J. Miao, X. Cao and C. Yang, *Adv. Mater.*, 2024, **36**, 2308314.
34 X.-C. Fan, K. Wang, Y.-Z. Shi, Y.-C. Cheng, Y.-T. Lee, J. Yu, X.-K. Chen, C. Adachi and X.-H. Zhang, *Nat. Photonics*, 2023, **17**, 280–285.
35 B. Lei, Z. Huang, S. Li, J. Liu, Z. Bin and J. You, *Angew. Chem., Int. Ed.*, 2023, **62**, e202218405.
36 X. Zeng, L. Wang, H. Dai, T. Huang, M. Du, D. Wang, D. Zhang and L. Duan, *Adv. Mater.*, 2023, **35**, 2211316.
37 J.-L. Brédas, D. Beljonne, V. Coropceanu and J. Cornil, *Chem. Rev.*, 2004, **104**, 4971–5004.
38 M. K. Etherington, J. Gibson, H. F. Higginbotham, T. J. Penfold and A. P. Monkman, *Nat. Commun.*, 2016, **7**, 13680.
39 P. K. Samanta, D. Kim, V. Coropceanu and J.-L. Brédas, *J. Am. Chem. Soc.*, 2017, **139**, 4042–4051.
40 K. Stavrou, A. Danos, T. Hama, T. Hatakeyama and A. Monkman, *ACS Appl. Mater. Interfaces*, 2021, **13**, 8643–8655.

© 2024 The Author(s). Published by the Royal Society of Chemistry